JOM, Vol. 68, No. 5, 2016
DOI: 10.1007/s11837-016-1861-x

Atomistic Modeling of Thermal Conductivity of Epoxy Nanotube Composites

NICHOLAS A. FASANELLA[1,2] and VEERA SUNDARARAGHAVAN[1,3]

1.—University of Michigan, Ann Arbor, MI 48109, USA. 2.—e-mail: nickfas@umich.edu. 3.—e-mail: veeras@umich.edu

The Green–Kubo method was used to investigate the thermal conductivity as a function of temperature for epoxy/single wall carbon nanotube (SWNT) nanocomposites. An epoxy network of DGEBA-DDS was built using the 'dendrimer' growth approach, and conductivity was computed by taking into account long-range Coulombic forces via a k-space approach. Thermal conductivity was calculated in the direction perpendicular to, and along the SWNT axis for functionalized and pristine SWNT/epoxy nanocomposites. Inefficient phonon transport at the ends of nanotubes is an important factor in the thermal conductivity of the nanocomposites, and for this reason discontinuous nanotubes were modeled in addition to long nanotubes. The thermal conductivity of the long, pristine SWNT/epoxy system is equivalent to that of an isolated SWNT along its axis, but there was a 27% reduction perpendicular to the nanotube axis. The functionalized, long SWNT/epoxy system had a very large increase in thermal conductivity along the nanotube axis (~700%), as well as the directions perpendicular to the nanotube (64%). The discontinuous nanotubes displayed an increased thermal conductivity along the SWNT axis compared to neat epoxy (103–115% for the pristine SWNT/epoxy, and 91–103% for functionalized SWNT/epoxy system). The functionalized system also showed a 42% improvement perpendicular to the nanotube, while the pristine SWNT/epoxy system had no improvement over epoxy. The thermal conductivity tensor is averaged over all possible orientations to see the effects of randomly orientated nanotubes, and allow for experimental comparison. Excellent agreement is seen for the discontinuous, pristine SWNT/epoxy nanocomposite. These simulations demonstrate there exists a threshold of the SWNT length where the best improvement for a composite system with randomly oriented nanotubes would transition from pristine SWNTs to functionalized SWNTs.

INTRODUCTION

Polymer-matrix composite materials are widely used in aerospace, automotive, marine and other high-performance applications due to their high specific strength, high specific stiffness, fatigue resistance, and ease of manufacturing. Thermoset polymers are the most predominant type of matrix system, and epoxies specifically are preferred for aerospace grade components due to their superior mechanical properties and resistance to environmental degradation due to moisture. However, epoxies are generally limited to low temperature applications, and this is in part due to their low thermal conductivity of ~0.24 W/mK at room temperature.[1] It is of great interest to improve the heat conduction in epoxies in order to remove excess heat, and boost reliability and performance. In this work, we demonstrate an integrated computational materials engineering (ICME) approach for assessing conductivity of epoxies with nano-additives that could help advance the development of high conductivity polymer composites. Specifically, we consider additives in the form of carbon nanotubes (CNTs). CNTs have very high thermal conductivity, with single wall carbon nanotubes (SWNTs) having a thermal conductivity of 1750–5800 W/mK[2,3] and high aspect ratios. The thermal conductivity of

(Published online March 16, 2016)

functionalized and pristine SWNT/epoxy nanocomposites will be investigated in this work using molecular dynamics (MD) simulations. The addition of SWNTs to epoxy has previously been shown to improve the mechanical and thermal dilatometric properties.[4] Inefficient phonon transport between nanotubes at discontinuities (i.e. the nanotube ends) is an important factor in the thermal conductivity of SWNT/epoxy nanocomposites, and for this reason discontinuous nanotubes are modeled in this study.

MD has been used in the past to study the thermal properties of simpler systems, such as metals, ionic salts and non-crosslinked amorphous polymers.[6–8] It is difficult to create accurate models for crosslinked polymers, and only recently has MD been used to study the thermal conductivity of these systems.[9,10] Thermal conductivity is generally calculated using equilibrium or non-equilibrium MD approaches. For equilibrium MD, the Green–Kubo method is used, which relates fluctuations of the thermal current to the thermal conductivity via the fluctuation-dissipation theorem.[5] For non-equilibrium MD (NEMD) methods, a long slab of polymer is constructed and a difference in temperature is established between a heat source and a sink at the ends of the slab and the flux is calculated. The epoxy in this study is built using the dendrimer growth approach which builds a cubic unit cell, and so is well suited for the Green–Kubo method. A comparison between the equilibrium Green–Kubo approach and NEMD method for an epoxy model built using multi-step crosslinking, found the two methods result in comparable values of thermal conductivity.[9]

MD studies of SWNT/polymer composites to this point have focused on the interfacial thermal conductance or resistance of SWNT/polymer systems. Shenogin et al. studied the effects of functionalization on transverse thermal transport properties in a SWNT/octane system using equilibrium MD. It was found the functionalization via chemical bonding greatly reduced the tube-matrix interfacial thermal resistance, and approximately doubled the effective composite conductivity.[11] Clancy and Gates used MD to study the effects of functionalization on the interfacial thermal resistance of a SWNT and bulk non-crosslinked poly(ethylene vinyl acetate) composite by grafting linear hydrocarbon chains to the surface of the SWNT. They found the interfacial thermal resistance decreased as the degree of functionalization (grafting density) and chain length of the grafted linear hydrocarbon chains increased. An analytic model using the calculated interfacial thermal resistance was used to calculate the effective thermal conductivity of the composite, which saw very large increases in thermal conductivity, approaching 100 W/mK for high grafting densities (.12 Å^2) of long nanotubes (100 μm) with high volume fractions (5%), and greater than 10 W/mK for many other combinations.[12] Huxtable et al. combined MD and experiments on a CNT-Octane system and found the thermal conductivity of the composite to be restricted by a low interfacial thermal conductance ($\sim$12 MW/m^2K).[13] Xu and Buehler used MD to show that the thermal junctions of two nanotubes can be improved by modifying the molecular structure via polymer wrapping of polyethylene chains and found improvement of up to 40% in thermal conductivity.[14] Alaghemandi et al. studied a composite of CNTs and polyamide-6,6 using reverse non-equilibrium MD and found that the thermal conductivity of the composite increased slightly parallel to the nanotube and decreased perpendicular to the nanotube. They concluded that the high interfacial thermal resistances, in the absence of chemical modification or any other alteration, was hindered by poor heat transfer from the polymer to the nanotubes.[15] Varshney et al. used non equilibrium MD to investigate the interfacial thermal conductance in functionalized CNT/epoxy composite system for crosslinked and non-crosslinked systems. The interface thermal conductance was 20% higher for the crosslinked system, and the increase in interface thermal conductance was shown to be linear with increasing degree of functionalization for both systems.[16] SWNTs that span the entire MD cell become infinite when periodic boundary conditions are applied. This, or the use of NEMD methods, has limited all of the aforementioned studies, with exception of Alaghemandi et al., to measuring the conductivity/resistance perpendicular to the nanotube axis. These studies have identified the the interfacial thermal resistance as the primary reason for lower than expected increases in the composite thermal conductivity.[11,14,15]

Experimentally, there have been a number of studies investigating the potential increase in thermal conductivity from adding SWNTs to epoxy. Experimental studies have generally shown a monotonic linear increase in the effective thermal conductivity as the loading of nanotubes increases when considering weight fractions of SWNTs. Gojny et al. studied epoxy/SWNT, epoxy/DWNT and epoxy/MWNT composites and the effects of functionalization on the DWNT and MWNT nanocomposites.[17] A 20% increase in thermal conductivity was seen at 0.5 wt.%. Biercuk et al. studied samples with 1 wt.% SWNT and saw a 125% increase in thermal conductivity at room temperature.[18] Liu and Fan showed that for 2 wt.% CNT (95% multiwall), chemical modification can reduce the interfacial thermal impedance in CNTs-plydimethylsiloxanerubber nanocomposites, but have negative effects on the thermal conductivity of the CNT itself.[19] At higher nanotube loading, 3 wt.% SWNT, Choi et al. saw thermal conductivity increase by up to 300%. They found the effective thermal conductivity can be further enhanced another 10% via magnetic alignment.[20] At 10% SWNTs by volume, Byring et al. saw up to 64% improvement in thermal conductivity.[21] The reviewed literature does not

show the existence of a thermal peculation threshold, where thermal transport properties are drastically increased at a certain CNT loading, at even at very high nanotube loading. This is in stark contrast to the electrical conductivity of CNT/epoxy composites where orders of magnitude increases are seen at the electric percolation threshold, which for SWNT/epoxy composites is only 0.05 wt.% SWNT.[22] Experimental results have yielded results far lower than what one would estimate from a rule of mixtures calculations given the high inherent CNT thermal conductivity.

Thus far, experimental results have not seen the improvements in thermal conductivity simulations have predicted possible, and inefficient phonon transport between nanotubes is likely the limitation.[23] The ends of the SWNT are discontinuities, and the phonon mean free path is approximately 0.5 μm for SWNTs at room temperature,[24] and so it can be expected phonon scattering will be significant at the free ends for nanotubes shorter than this length. Previous MD studies have been limited to calculating the interfacial thermal resistance or conductivity due to the lack of a free boundary. This will prevent boundary scattering, and the only scattering mechanism will be phonon–phonon interactions. In this study, equilibrium MD simulations were performed on the an epoxy model created using the dendrimer growth approach. Functionalized and pristine nanotube/epoxy composites are created for various nanotube lengths, and the thermal conductivity of the systems was calculated via the Green–Kubo formulation in 3D. Covalent functionalization was explored to improve the interfacial thermal conductivity, though it was expected to decease the inherent SWNT conductance.[11] The methods used to create the material systems are outlined in "Material Modeling" Section. For systems with short-range pair interactions, such as the Lennard–Jones or embedded atom potential, the heat flux expression in the integrand of the Green–Kubo is well known. Electrostatic forces between partial charges on atoms lead to long range interactions. Hence, the per-atom energy to compute the heat flux vector in the case of long range interatomic interactions is calculated on a periodic domain using the standard or mesh-based particle-particle-particle-mesh (PPPM) Ewald methods.[25] In "Green–Kubo method for predicting thermal conductivity" Section, we explore 'k-space' or 'reciprocal' modeling of electrostatic energy. Results with and without this long range correction are shown and compared with experiments in the "Results" Section, and a summary of the results is given in the "Conclusion" Section. To the author's best knowledge, for the first time in literature we will be using MD to study discontinuous nanotubes in epoxy composites to factor in nanotube end effects to the thermal conductivity of SWNT/epoxy nanocomposites.

MATERIAL MODELING

A common epoxy, Diglycidyl ether of bisphenol A (DGEBA) was chosen for this study. The DGEBA was crosslinked with curing agent 3–3' diamino diphenyl sulfone (DDS). The epoxy and amine structures are shown in Fig. 1. Each epoxide has a crosslinking functionality of one towards the amine curing agents. The epoxy monomer has two epoxide (oxirane ring) groups leading to a total functionality of two. Each amine group has a functionality of two towards epoxy molecules. The DDS monomer has two amine groups and a total functionality of four. A typical amine stoichiometric ratio for synthetic epoxy is approximately 2:1 or 33.3 mol.% amine. The polymer is formed by bonding the epoxide group in DGEBA to the amine groups in the DDS. To form a crosslink, the primary amine group reacts with the epoxide group, creating a bond between the terminal carbon of the epoxide group and the nitrogen of DDS. The carbon-oxygen bond breaks between the terminal carbon and oxygen from the epoxide, and forms and alcohol (–OH) link. The crosslinked structure seen in Fig. 2a can undergo another reaction with a different epoxy molecule, forming the final crosslinked structure shown in Fig. 2b.

A major hurdle in creating accurate models for molecular simulation of industrial grade epoxies is attaining realistic crosslinking densities, where a conversion of 70–95% is typically seen when measured through Near-Infrared (NIR) Spectroscopy.[26] A number of approaches have been employed to build crosslinked polymer networks with greater than 70% crosslink conversions. The majority of these approaches can be characterized based on whether unreacted monomer mixtures are crosslinked all-at-once (one-step) or over time (multi-step). For one-step crosslinking, sites are first randomly selected and then pairs of sites within a capture radius are crosslinked together.[27,28] In multi-step crosslinking, every reactive pair that satisfies a length criteria are crosslinked iteratively, with equilibration and the length criteria increasing with every iteration.[29,30] Multi-step methods prevents and relieves network strains, but they are computationally expensive. A new method was introduced by Christensen in 2007 to build epoxy networks using a 'dendrimer' growth approach.[31,32] In this method, the thermoset resin is modeled by starting with a single monomer and then crosslinking a second layer of monomers around it. In the next step, a third layer of monomers are crosslinked to the second layer. In this way, generations (layers) of monomers are added to a seed structure that grows in size at every pass. The principal advantages of the dendrimer growth method are the low computational cost of the growing procedure, and the complete avoidance of artificial network strain during curing.

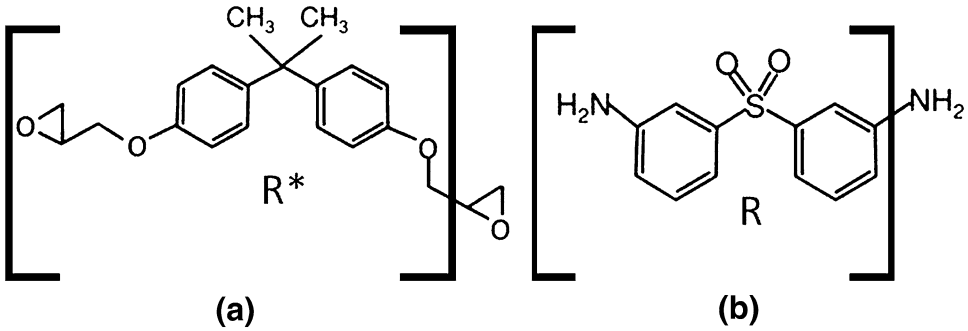

Fig. 1. (a) Chemical structure of epoxy resin, DGEBA and (b) the amine monomer diamino diphenyl sulfone. Brackets give the notation for R and R* in Fig. 2.

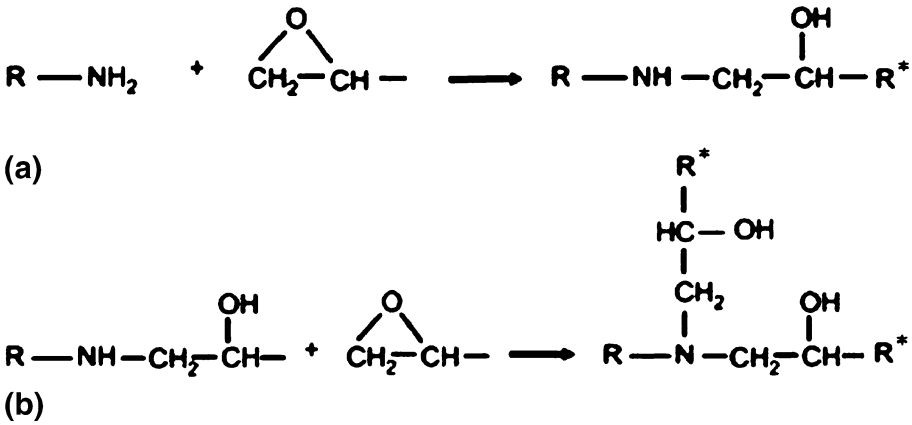

Fig. 2. (a) Epoxy primary reaction with amine NH_2 group (b) Second reaction of NH group with epoxy to completely crosslink the hardener.

The 'dendrimer' growth approach was used to build the epoxy network in Materials Studio[33] shown in Fig. 3. The network contains 36 amine groups and 71 epoxy groups, leading to total 4601 atoms. The system has been shown to be sufficiently complex to accurately capture the amorphous nature of the polymer. Previously for the epoxy model, the dilatometric curve was shown to match experimental results: the experimental glass transition temperature was matched, the full elastic stiffness matrix was generated, the structure was verified to be isotropic, and the proper density was obtained.[4] All simulations in this work are performed under periodic boundary conditions, and the Consistent Valence Force Field (CVFF)[34] potential was used for bonded and non-bonded interactions in LAMMPS.[35] CVFF has been used in previous studies to accurately predict thermodynamic properties of epoxy[9,10] 75% of available epoxy sites were crosslinked, which is realistic for many structural epoxies.

The structure was equilibrated via a sequence of energy minimization and annealing. The dendrimer structure was optimized by minimizing the energy via conjugate gradient (CG) minimization for 10,000 iterations. Next, MD was used to anneal the structure using an NPT ensemble. Dynamics was first performed well above glass transition temperature

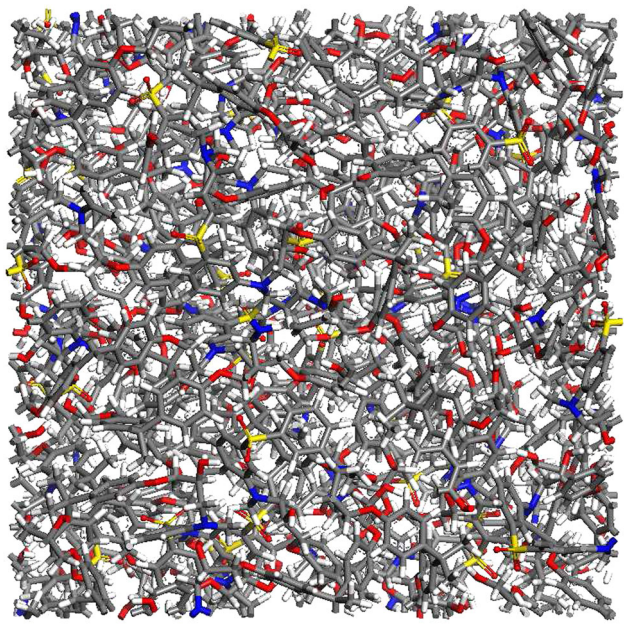

Fig. 3. The dendrimer structure of epoxy shown in a cell after energy minimization.

(600 K and 1 atm) for 500 ps. Next, dynamics was run well below T_g (1 K and 1 atm) for 500 ps, followed by CG. After ten cycles, the density

converged to within 0.5% across consecutive annealing steps. A density of 1.17 g/cc at 1 atm and 1 K was obtained after convergence. CNT/Epoxy nanocomposites were built by creating a vacancy in the epoxy by radially moving atoms outward and inserting a SWNT (4,4) into the space. Moving atoms caused bonds to displace from their equilibrated length, so it was necessary to equilibrate the structure via the same annealing process ran previously via a sequence of CG minimization and dynamics above and below T_g.

Functionalization of the SWNT/Epoxy composites was achieved by creating a covalent bond between the SWNT and the amine. The DDS molecule contains two amine groups, one of which was bonded to the SWNT. As seen in Fig. 4a, the nanotube is attached to the DDS, and the other amine group bonds with the epoxide as shown previously in Fig. 2. Amine that were previously unreacted were chosen to bond to the SWNT, so this method of functionalization does not effect the epoxy's degree of crosslinking. Again, bonds were displaced from their equilibrium length so equilibration was performed via a sequence of the conjugate gradient (CG) minimization and annealing until the density was seen to converge. The functionalized system contains four covalent bonds, and the equilibrated structure is seen in Fig. 4b. When the nanotube spans the entire cell, the use of periodic boundary conditions leads to the creation of an infinite nanotube, shown in Fig. 5a, where two periodic cells are shown in the 'y' and 'z' directions. Realistically, nanotubes are not infinite and so end effects are important. For this reason, nanotubes that do not span the entire cell are also created using this same method, and the equilibrated structure in Fig. 5b shows epoxy filling in the space between the periodic nanotubes.

GREEN–KUBO METHOD FOR PREDICTING THERMAL CONDUCTIVITY

The Green–Kubo method is an equilibrium MD approach that calculates the thermal conductivity (K) from the fluctuations of the heat current along a direction, J_x, via the fluctuation-dissipation theorem.[5,36] The thermal conductivity is given by

$$K = \frac{V}{k_B T^2}\int_0^{\infty} \langle J_x(t) J_x(0)\rangle dt \tag{1}$$

where V and T are the volume and temperature of the system respectively, and k_B is the Boltzmann constant. $\langle J_x(t)J_x(0)\rangle$ is the heat current auto correlation function (HCACF).

For an isotropic material, a scalar conductivity is obtained by averaging across all three directions. For neat epoxy in the the present study, the following formula is employed where the factor of three in the denominator arises due to the averaging across the x, y and z directions.

$$K = \frac{V}{3k_B T^2}\int_0^{t_c} \langle \boldsymbol{J}(t)\boldsymbol{J}(0)\rangle_{t_s} dt \tag{2}$$

In the above expression, $\boldsymbol{J}$ is the heat current vector, t_c stands for the finite correlation time over which the integration is carried out, and t_s is the sampling time for which the ensemble average for computing HCACF is accumulated. Since the nanocomposite systems are not isotropic, it is not possible to average over all three directions and so the thermal conductivity is calculated for each direction individually.

The heat current vector is defined in a a number of different ways.[37] It is most commonly defined as:

$$\boldsymbol{J} = \frac{1}{V}\frac{d}{dt}\sum_{i=1}^{N} \boldsymbol{r}^i e^i \tag{3}$$

where, $\boldsymbol{r}^i$ and e^i are the position vector and total energy of atom i, respectively. The summation is done over the total number of atoms in the system, N. The energy of atom i, e^i, is obtained by summing the potential energy (PE) and kinetic energy (KE):

$$e^i = \frac{1}{2} m^i \|\boldsymbol{v}^i\|^2 + U^i \tag{4}$$

where m^i and $\boldsymbol{v}^i$ are the mass and velocity of atom i, respectively. U^i is the potential energy of atom i. It is dependent on the form of interaction potential (includes bonded and non-bonded interactions) used in the simulations. In the CVFF potential, the total energy is computed as a sum of pair interactions (U_{pair}), Coulombic interactions ($U_{coulomb}$), energies that accounts for changes in bond lengths (U_{bond}), bond angle (U_{angle}), dihedral angle ($U_{dihedral}$) and improper dihedral angle ($U_{improper}$) in the following form:

$$U = U_{pair} + U_{coulomb} + U_{bond} + U_{angle} + U_{dihedral} + U_{improper} \tag{5}$$

The per-atom energy (U^i) is computed by averaging the energy contributions and distributing an equal portion to each the atom the interaction set. For example, a quarter of the dihedral energy is assigned to each of the four atoms in the dihedral term.

$$\begin{aligned} U^i = &\left[\frac{1}{2}\sum_{n=1}^{N_p} U_{pair}(\boldsymbol{r}^i, \boldsymbol{r}^2) + \frac{1}{2}\sum_{n=1}^{N_b} U_{bond}(\boldsymbol{r}^i, \boldsymbol{r}^2) + \frac{1}{3}\sum_{n=1}^{N_a} U_{angle}(\boldsymbol{r}^i, \boldsymbol{r}^2, \boldsymbol{r}^3)\right] \\ &+ \left[\frac{1}{4}\sum_{n=1}^{N_d} U_{dihedral}(\boldsymbol{r}^i, \boldsymbol{r}^2, \boldsymbol{r}^3, \boldsymbol{r}^4) + \frac{1}{4}\sum_{n=1}^{N_i} U_{improper}(\boldsymbol{r}^i, \boldsymbol{r}^2, \boldsymbol{r}^3, \boldsymbol{r}^4 + \frac{1}{2}\sum_{n=1}^{N_c} U_{coulomb}(\boldsymbol{r}^i, \boldsymbol{r}^2)\right] \end{aligned} \tag{6}$$

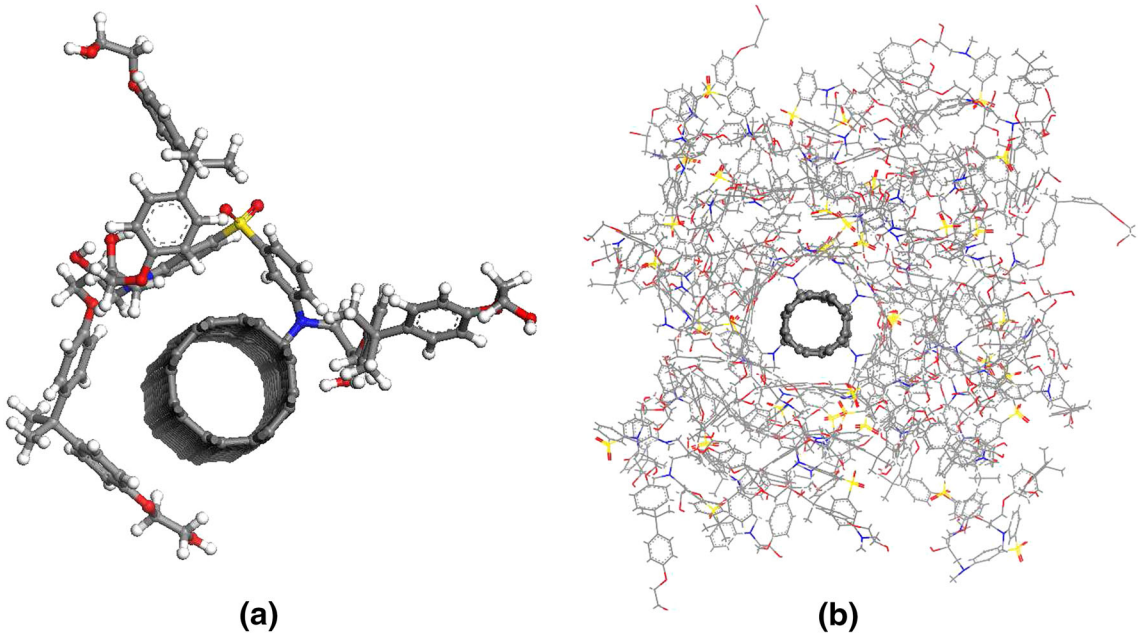

Fig. 4. (a) Nanotube functionalization to amine and subsequent crosslinking to epoxy. (b) Functionalized carbon nanotube and epoxy nanocomposite.

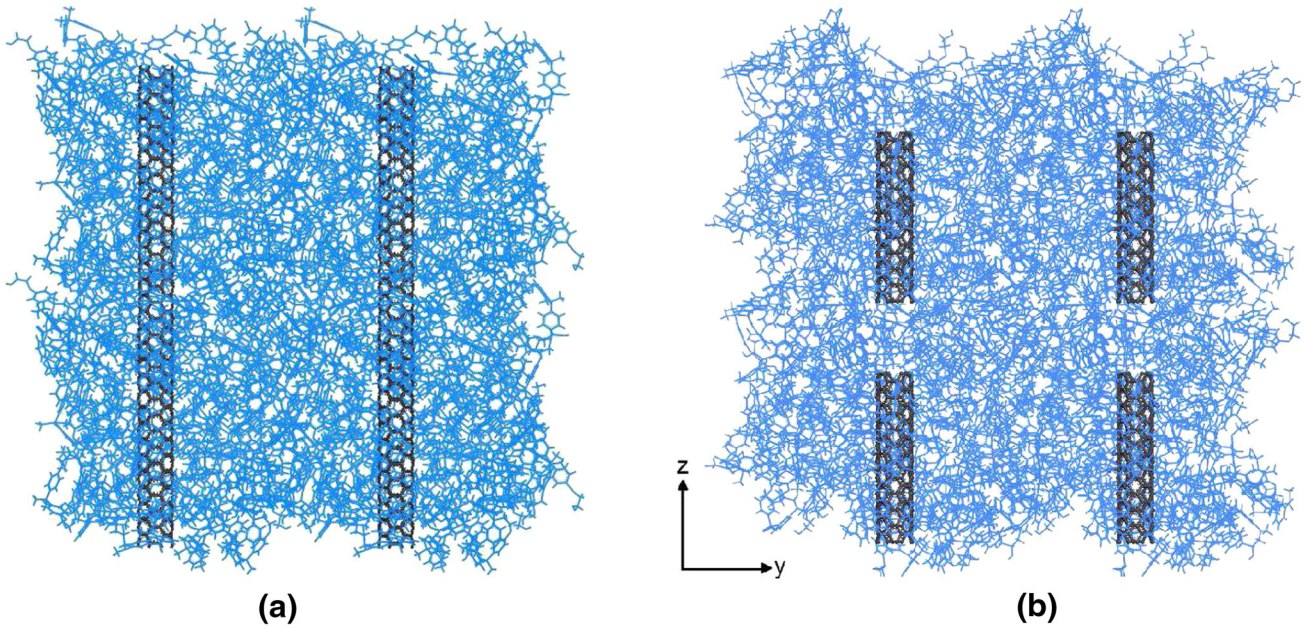

Fig. 5. Two periodic cells are shown in the *z*-direction and *y*-direction to show nanotube spacing for (a) nanotubes that span the entire cell that effectively become infinite and (b) discontinuous nanotubes that span 11/15 of the cell.

The first term in the above expression is the pairwise energy contribution, where n goes over the N_p atoms neighboring atom i, and $\boldsymbol{r}^i$ and $\boldsymbol{r}^2$ are the positions the two atoms in the pairwise interaction. The second term is a bond contribution of similar form for the N_b bonds containing atom i. The third, fourth and fifth terms are similar expressions for the N_a angle, N_d dihedral, and N_i improper interactions, respectively, that atom i is part of. The sixth term, $U_{coulomb}$, is the contribution from long-range Columbic interactions and are handled differently using the standard or PPPM Ewald methods described in the next section.

Substituting Eq. 4 in Eq. 3 and differentiating with respect to time, the microscopic heat current vector $\boldsymbol{J}$ is obtained as:

$$\boldsymbol{J}(t) = \frac{1}{V}\sum_{i=1}^{N} \boldsymbol{v}^i e^i + \sum_{i=1}^{N} \boldsymbol{S}^i \cdot \boldsymbol{v}^i \tag{7}$$

The first term is the diffusive part of the heat current which is caused by motion of atoms. The second term is the interaction part of the heat current which represents the transfer of energies due to interatomic interactions, where $\boldsymbol{S}^i$ is the the per atom stress tensor. For the CVFF potential, the stress tensor for atom i ($\boldsymbol{S}^i$) is the following expression, where a and b iterate over the values x,y,z to generate the 6 components of the symmetric tensor:

$$\begin{aligned} V\boldsymbol{S}^i_{ab} = &\left[\frac{1}{2}\sum_{n=1}^{N_p}(\boldsymbol{r}^i_a\boldsymbol{F}^i_b + \boldsymbol{r}^2_a\boldsymbol{F}^2_b) + \frac{1}{2}\sum_{n=1}^{N_c}(\boldsymbol{r}^i_a\boldsymbol{F}^i_b + \boldsymbol{r}^2_a\boldsymbol{F}^2_b)\right. \\ &\left. + \frac{1}{2}\sum_{n=1}^{N_b}(\boldsymbol{r}^i_a\boldsymbol{F}^i_b + \boldsymbol{r}^2_a\boldsymbol{F}^2_b)\right] \\ &+ \left[\frac{1}{3}\sum_{n=1}^{N_a}(\boldsymbol{r}^i_a\boldsymbol{F}^i_b + \boldsymbol{r}^2_a\boldsymbol{F}^2_b + \boldsymbol{r}^3_a\boldsymbol{F}^3_b)\right. \\ &\left. + \frac{1}{4}\sum_{n=1}^{N_d}(\boldsymbol{r}^i_a\boldsymbol{F}^i_b + \boldsymbol{r}^2_a\boldsymbol{F}^2_b + \boldsymbol{r}^3_a\boldsymbol{F}^3_b + \boldsymbol{r}^4_a\boldsymbol{F}^4_b)\right] \\ &+ \left[\frac{1}{4}\sum_{n=1}^{N_i}(\boldsymbol{r}^i_a\boldsymbol{F}^i_b + \boldsymbol{r}^2_a\boldsymbol{F}^2_b + \boldsymbol{r}^3_a\boldsymbol{F}^3_b + \boldsymbol{r}^4_a\boldsymbol{F}^4_b)\right] \end{aligned} \tag{8}$$

In the first three terms, $\boldsymbol{F}^i$ and $\boldsymbol{F}^2$ are the forces resulting from two atoms interacting. Similarly, there are forces due to the angle, dihedral, and improper interactions of atom i. The above stress tensor contains only the virial terms and does not include the kinetic energy contribution.

Computation of Long Range Coulombic Interactions

In cross-linked polymers, there are long range interatomic interactions due to electrostatic forces between partial charges on atoms. In this case, the energy contribution per atom required for the computation of the heat current vector is more conveniently calculated on a periodic domain using the standard or mesh-based PPPM Ewald methods. In these methods, a 'real-space' component of electrostatic energy is computed within a small cut-off distance, beyond which the slow decay is modeled using the 'k-space' or 'reciprocal' part, which decays with the inverse distance. The Ewald expression for potential energy $U_{coulomb}$ and its contribution to the stress tensor are computed in this section. In the Ewald approach, the electrostatic potential energy of a neutral distribution of N atoms with point charges q_i can be written as:[38]

$$\begin{aligned} 4\pi\epsilon_0 U_{coulomb} &= \frac{1}{2}\sum_{i=1}^{N}\sum_{\substack{j=1 \\ j\neq i}}^{N}\frac{q_i q_j}{r_{ij}} \\ &= \frac{1}{2}\sum_{i=1}^{N}\sum_{\substack{j=1 \\ j\neq i}}^{N}\frac{q_i q_j}{r_{ij}} erfc(\kappa r_{ij}) \\ &+ \frac{2\pi}{V}\sum_{k\neq 0}\frac{exp(k^2/4\kappa^2)}{k^2} \\ &\sum_{i=1}^{N}\sum_{\substack{j=1 \\ j\neq i}}^{N} q_i q_j exp(i\boldsymbol{k}\cdot\boldsymbol{r}_{ij}) \end{aligned} \tag{9}$$

In Eq. 9, ϵ_0 is the electric permittivity of free space, and $r_{ij} = |\boldsymbol{r}_j - \boldsymbol{r}_i|$ is the distance between charges i and j. $erfc(\kappa r_{ij})$ is the complimentary error function of the distance multiplied by a convergence factor κ, and the second term on the right-hand side is the Fourier expansion of the difference between the first term and the full electrostatic potential energy. The Fourier expansion in terms of wave vectors $k_\alpha = \frac{2\pi n_\alpha}{L}$ (α = x, y, z) is used where L is the periodic box size. Also, The k-space part of the electrostatic potential energy and the stress tensor, in addition to a sum over wave vectors $\boldsymbol{k}$, contains double sums over all pairs of atoms i,j; i≠j. Observing that $\boldsymbol{r}_{ij} = \boldsymbol{r}_j - \boldsymbol{r}_i$, this double sum can be written as a single sum over N charges which speeds up the computation by N-fold.[39]

$$\begin{aligned} &\sum_{i=1}^{N}\sum_{\substack{j=1 \\ j\neq i}}^{N} q_i q_j exp(i\boldsymbol{k}\cdot\boldsymbol{r}_{ij}) \\ &= \sum_{i=1}^{N} q_i exp(i\boldsymbol{k}\cdot\boldsymbol{r}_i)\sum_{j=1}^{N} q_j exp(-i\boldsymbol{k}\cdot\boldsymbol{r}_j) \\ &- \sum_{i=1}^{N}(q_i)^2 = \Theta(\boldsymbol{k})\Theta(-\boldsymbol{k}) - \sum_{i=1}^{N}(q_i)^2 \end{aligned} \tag{10}$$

Here, $S(\boldsymbol{k})$ is the structure factor given as $\Theta(\boldsymbol{k}) = \sum_{i=1}^{N} q_i exp(i\boldsymbol{k}\cdot\boldsymbol{r}_i)$. The sum of the squared charges is subtracted because the first term on the right-hand side contains the self-interaction term with $i = j$. With the use of the transformation (10), the expression for the electrostatic potential energy is

$$4\pi\epsilon_0 U_{coulomb} = \frac{1}{2}\sum_{i=1}^{N}\sum_{\substack{j=1 \\ j\neq i}}^{N}\frac{q_i q_j}{r_{ij}}erfc(\kappa r_{ij}) - \frac{\kappa}{\pi^{1/2}}\sum_{i=1}^{N}(q_i)^2 + \frac{2\pi}{V}\sum_{k\neq 0}\frac{exp(k^2/4\kappa^2)}{k^2}\Theta(\boldsymbol{k})\Theta(-\boldsymbol{k}) \quad (11)$$

The subtracted term $(\frac{\kappa}{\pi^{1/2}})\sum_{i=1}^{N}(q_i)^2$, corresponding to i=j, is the contribution due to self-interaction. The per atom version of the potential energy contribution is calculated using a per atom structure factor $\Theta^i(\boldsymbol{k})$ defined as $\Theta^i(\boldsymbol{k}) = q_i exp(i\boldsymbol{k}\cdot\boldsymbol{r}_i)$ as follows:

$$4\pi\epsilon_0 (U^i)_{coulomb} = \frac{1}{2}\sum_{\substack{j=1 \\ j\neq i}}^{N}\frac{q_i q_j}{r_{ij}}erfc(\kappa r_{ij}) - \frac{\kappa}{\pi^{1/2}}(q_i)^2 + \frac{2\pi}{V}\sum_{k\neq 0}\frac{exp(k^2/4\kappa^2)}{k^2}\Theta^i(\boldsymbol{k})\Theta(-\boldsymbol{k}) \quad (12)$$

The elements of the Coulombic part of the stress tensor are obtained by the differentiation of Eq. 11 with respect to components of $\boldsymbol{r}_{ij}$. The resulting electrostatic part of the stress tensor $(\boldsymbol{S}_{ab})_{coulomb}$ is given as follows, where a and b take on values x,y,z to generate the 6 components of the symmetric tensor:[40]

$$\begin{aligned} 4\pi\epsilon_0 V(\boldsymbol{S}_{ab})_{coulomb} &= \frac{1}{2}\sum_{i=1}^{N}\sum_{\substack{j=1 \\ j\neq i}}^{N}\frac{q_i q_j}{r_{ij}^3}r_{ija}r_{ijb} \\ &= \frac{1}{2}\sum_{i=1}^{N}\sum_{\substack{j=1 \\ j\neq i}}^{N} q_i q_j \left[\frac{erfc(\kappa r_{ij})}{r_{ij}^3} + \frac{2\kappa}{\pi^{1/2}}\frac{exp(-\kappa^2 r_{ij}^2)}{r_{ij}^2}\right] r_{ija}r_{ijb} \\ &\quad + \frac{2\pi}{V}\sum_{k\neq 0}\frac{exp(k^2/4\kappa^2)}{k^2}\left[\delta_{ab} - 2\left(\frac{1}{k^2}+\frac{1}{4\kappa^2}\right)k_a k_b\right]\Theta(\boldsymbol{k})\Theta(-\boldsymbol{k}) \end{aligned} \quad (13)$$

where $\delta_{\alpha\beta}$ is the Kronecker symbol. The per atom stress tensor is computed using the per atom structure factor as:

$$\begin{aligned} 4\pi\epsilon_0 V(\boldsymbol{S}_{ab})^i_{coulomb} &= \frac{1}{2}\sum_{\substack{j=1 \\ j\neq i}}^{N}\frac{q_i q_j}{r_{ij}^3}r_{ija}r_{ijb} \\ &= \frac{1}{2}\sum_{\substack{j=1 \\ j\neq i}}^{N} q_i q_j \left[\frac{erfc(\kappa r_{ij})}{r_{ij}^3} + \frac{2\kappa}{\pi^{1/2}}\frac{exp(-\kappa^2 r_{ij}^2)}{r_{ij}^2}\right] r_{ija}r_{ijb} \\ &\quad + \frac{2\pi}{V}\sum_{k\neq 0}\frac{exp(k^2/4\kappa^2)}{k^2}\left[\delta_{ab} - 2\left(\frac{1}{k^2}+\frac{1}{4\kappa^2}\right)k_a k_b\right]\Theta^i(\boldsymbol{k})\Theta(-\boldsymbol{k}) \end{aligned} \quad (14)$$

The PPPM solver employs the same approach as the standard Ewald approach described above, but is more accurate, and the atomic charges are mapped to a 3D mesh and fast Fourier transforms (FFTs) are used to compute the structure factors.[41]

RESULTS

A preliminary convergence study was done using a Lennard–Jones/Coloumb interaction cutoff of 12.5 Å to find the necessary sampling and correlation times. The structures were equilibrated at the temperature being studied for 0.5 ns, followed by further equilibration and collection of heat current data used for calculation of the autocorrelation function. A correlation time of 8 ps is initially used, and the sampling interval was taken as the size of the timestep (1 fs). Convergence of the HCACF at 298K and 1 atm for neat epoxy is shown in Fig. 6. Sampling times longer than 0.8 ns were carried out but showed no significant further convergence of the HCACF. Figure 6b shows a zoomed in section of Fig. 6a, and here it can be seen that the variation in the HCACF is very small at 0.8 ns for neat epoxy. The effect of temperature on the HCACF convergence for a sampling time of 0.8 ns is shown in Fig. 7a. Even at higher temperatures, such as 423 K, good convergence of the HCACF was seen. Figure 7b shows the convergence error for the HCACF by comparing the value at the current sampling time with the HCACF value at a sampling time of 0.096 ns. As the timestep exceeds 0.8 ns, the error flattens out and the HCACF converges. Figures 6 and 7 show that a correlation time of 8 ps and a sampling time of 0.8 ns are sufficient for convergence of the HCACF in the temperature range of interest for neat epoxy. For the pristine and functionalized SWNT/epoxy nanocomposites, a correlation time of 16 ps is used because HCACF did not

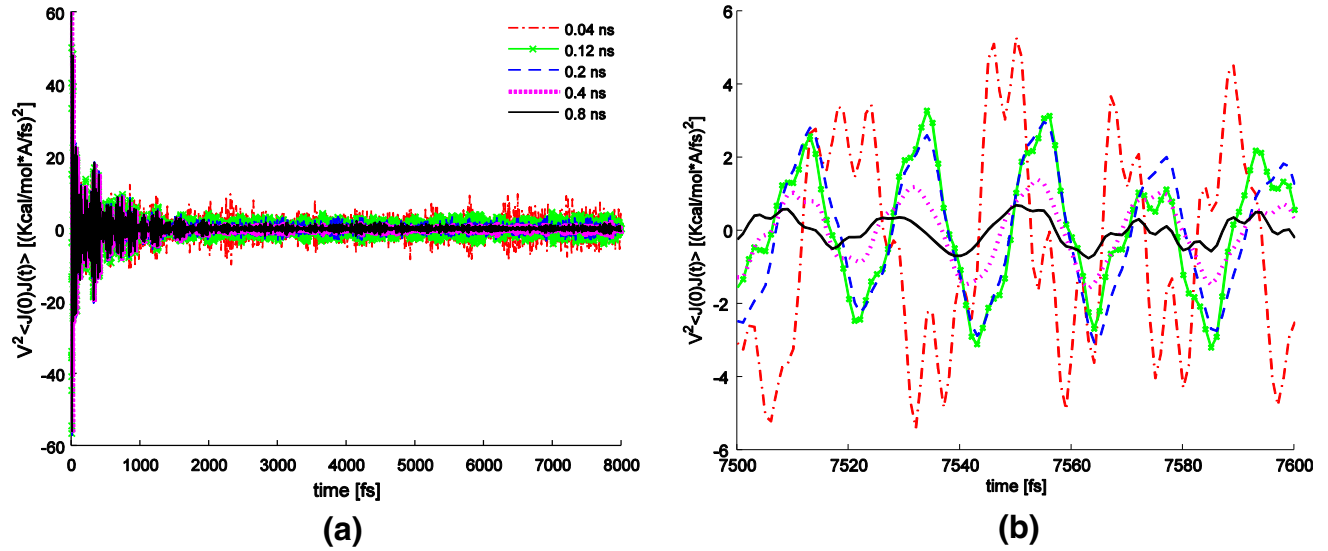

Fig. 6. (a) HCACF for neat epoxy at $T = 298$ K, $P = 1$ atm at different sampling times. (b) Zoomed HCACF for neat epoxy at $T = 298$ K, $P = 1$ atm to show convergence.

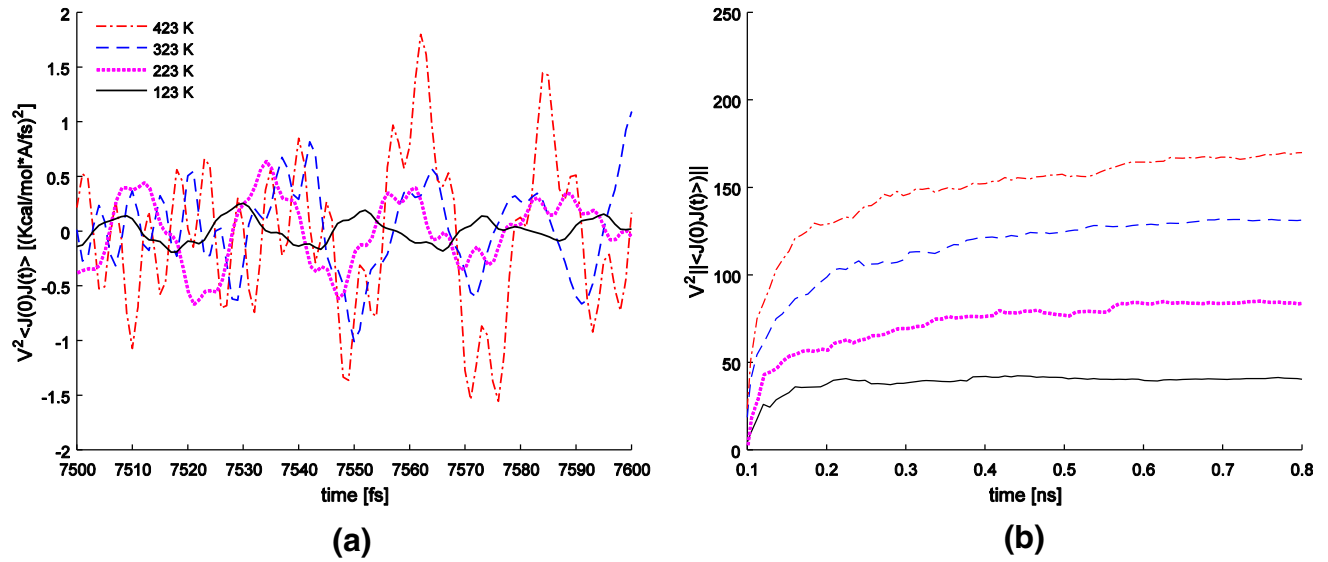

Fig. 7. (a) Zoomed in HCACF of neat epoxy for sampling time of 0.8 ns at various temperatures and $P = 1$ atm. (b) Convergence of HCACF at various temperatures and $P = 1$ atm.

show sufficient convergence for a correlation time of 8 ps. Convergence of the HCACF for the pristine SWNT/epoxy nanocomposite and functionalized SWNT/epoxy nanocomposite are shown in Figs. 8 and Fig. 9, respectively. Here, sampling times of 0.032 ns to 1.6 ns are compared. Convergence is seen to occur by 1.6 ns in Figs. 8b and 9b for the pristine SWNT/epoxy nanocomposite and functionalized SWNT/epoxy nanocomposite, respectively. This convergence study allowed us to determine the necessary correlation and sampling times for the three systems investigated.

Thermal conductivity for the epoxy as a function of temperature with and without long range corrections is shown in Fig. 10. The data labeled 'no long range correction' was a real-space algorithm and therefore did not include any long range Coulombic interactions. The red line, labeled 'With Long Range Correction' included the 'k-space' component electrostatic energy. The free parameters such as the grid size, and convergence acceleration factor are determined by specifying an accuracy value.[42] Here, an accuracy value was taken as 10^{-4}, meaning the error will be 1/10,000 of the force two unit point charges with a 1 Å separation exert on one other. Due to oscillations in the thermal conductivity results, all the reported values of thermal conductivity were averaged over 0.2 ns. Both measures of thermal conductivity, with and without long-range electrostatic forces have virtually identical slopes.

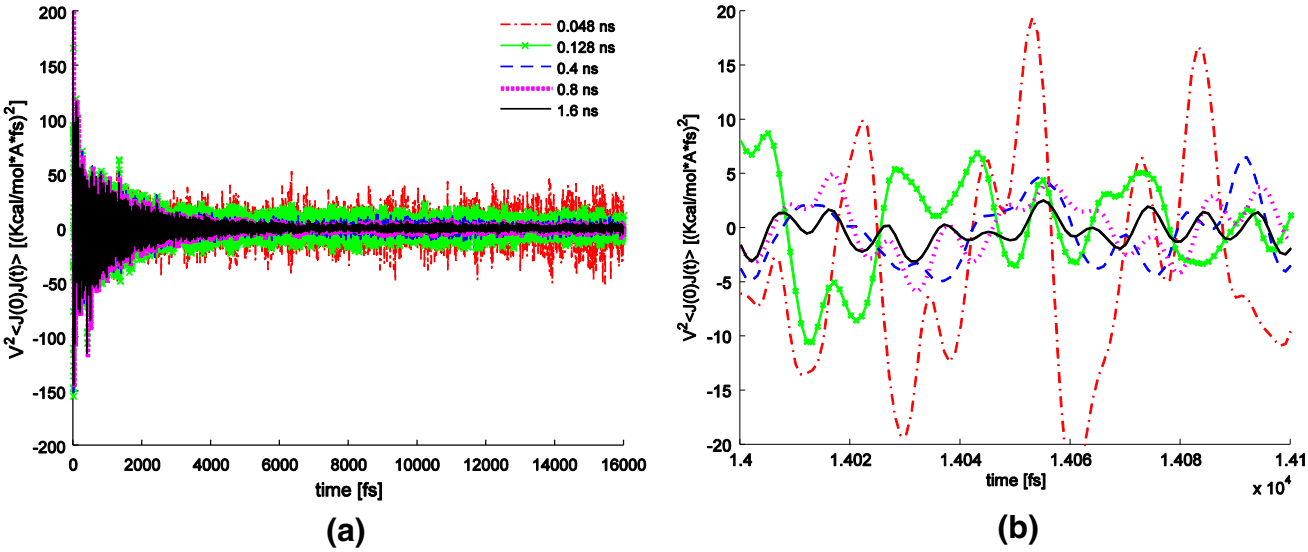

Fig. 8. (a) HCACF of pristine SWNT/epoxy nanocomposite at $T = 298$ K, $P = 1$ atm. (b) Zoomed HCACF of pristine SWNT/epoxy nanocomposite at $T = 298$K, $P = 1$ atm to show convergence.

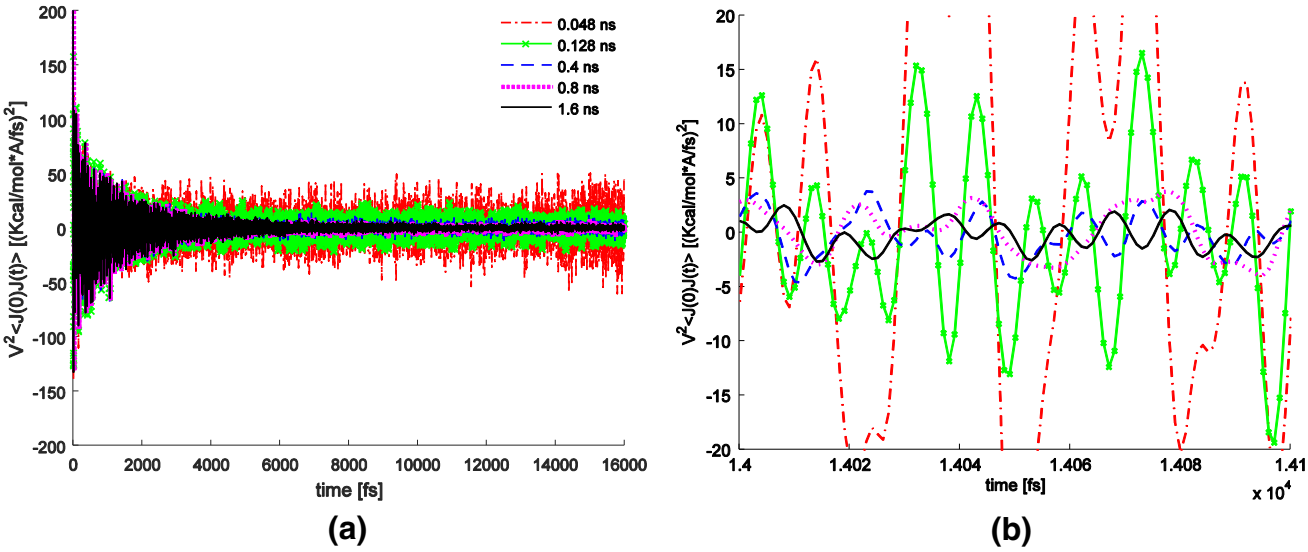

Fig. 9. (a) HCACF of functionalized SWNT/epoxy nanocomposite at $T = 298$ K, $P = 1$ atm. (b) Zoomed HCACF of functionalized SWNT/epoxy nanocomposite at $T = 298$ K, $P = 1$ atm to show convergence.

However, at room temperature the PPPM method matches the experimental value of epoxy, while the LJ-cutoff overestimates it by approximately 50%. Figure 11a shows the convergence of thermal conductivity to 0.24 W/mK for a PPPM simulation, which is in excellent agreement with experimental values for DGEBA-based epoxy at room temperature.[1,9,10] Sampling times as long as 3.2 ns have been investigated, but due to the numerical integration of the HCACF in the thermal conductivity calculation, there will be a steady drift after convergence. This is shown in Fig. 11b, where convergence occurred between 1 ns and 1.5 ns. As the sample time moves past the converged region, the thermal conductivity is seen to steadily drift upwards away from the converged value.

Fig. 10 shows the necessity of including long range interactions; and how they allow the thermal conductivity to accurately capture experimental values. The PPPM method was used to calculate the thermal conductivity of pristine and functionalized SWNT/epoxy nanocomposites. The first system investigated was an isolated SWNT that spanned the entire simulation cell. The thermal conductivity of a nanotube of length 36.89 Å with the application of periodic boundary conditions (making the SWNT

length effectively infinite) is shown in Fig. 12. As expected, the nanotube shows decreasing thermal conductivity with increasing temperature.[43] Compared to many studies, the thermal conductivity of the nanotube along the nanotube length is significantly less.[2,3] It has been seen previously that there is a length dependence in the thermal conductivity of nanotubes even with periodic boundary conditions.[44] Longer nanotubes allow additional modes with smaller wave vectors. Smaller wave vectors are longer lived than the higher frequency modes due to a lower probability of Umklapp scattering, and generally have higher group velocities, leading to an increased thermal conductivity.[44]

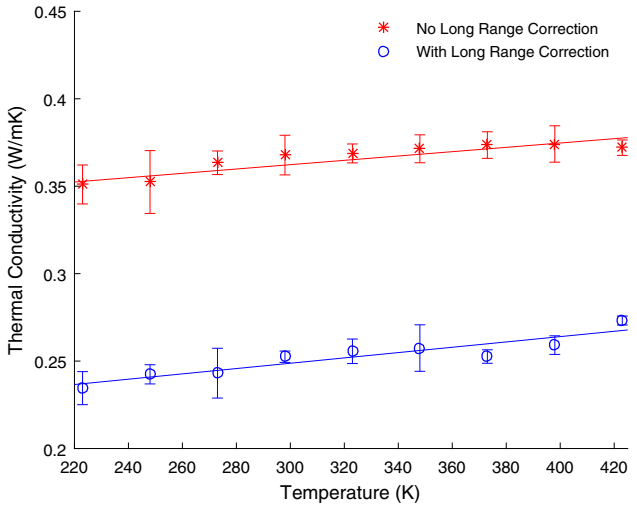

Fig. 10. Thermal conductivity for neat epoxy with and without long range electrostatic interactions for various temperatures at 1 atm.

The thermal conductivity in the plane perpendicular to the nanotube (x–y) for both the pristine and functionalized nanocomposites systems, compared with neat epoxy is shown in Fig. 13. The pristine SWNT/epoxy nanocomposite's thermal conductivity does not show much variation with temperature, and is reduced by 27% at room temperature in the x–y plane when compared to isotropic neat epoxy. This reduction is due to there being less degrees of freedom per unit volume available for heat transport, since this occurs predominately in the polymer and is therefore hindered by the inclusion of the nanotube.[15] The Van der Waal forces are inefficient in thermal transport across the SWNT-epoxy interface, and most of the heat flux occurs in the polymer since heat transfer is slow through the hollow tube. The thermal conductivity of the functionalized SWNT/epoxy system shows a stronger temperature dependence, and is greater than that of neat epoxy over the entire temperature range, with a 64% improvement at room temperature. The increase in the thermal conductivity in the interface direction is due to an improved thermal coupling between the SWNT and the epoxy. The creation of sp^3 hybridization defects in functionalization creates scattering sites for phonons along the SWNT, allowing energy to be transferred from the epoxy to the SWNT.

The thermal conductivity parallel to the nanotube (z-direction) for the pristine SWNT/epoxy and functionalized SWNT/epoxy nanocomposites are shown in Fig. 14a and b. Figure 14a shows very large improvements along the nanotube direction for the pristine SWNT/epoxy system over neat epoxy, much more so than the functionalized system. The pristine SWNT/epoxy system demonstrates a thermal conductivity along the SWNT direction equivalent to that of an isolated nanotube, as demonstrated

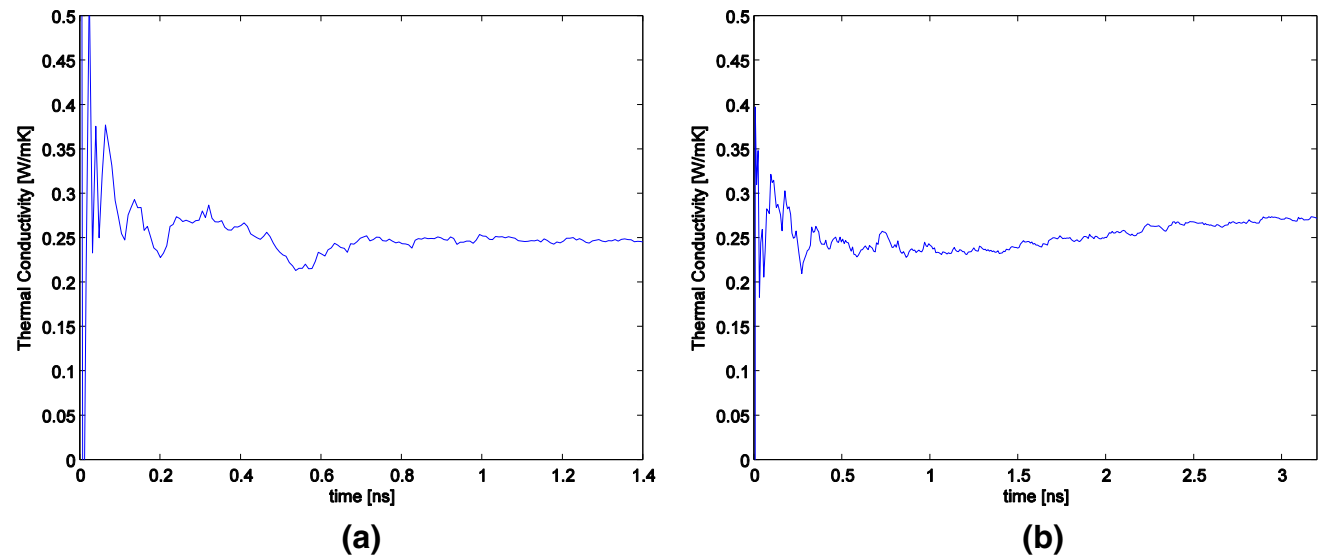

Fig. 11. (a) Convergence of the thermal conductivity at $T = 298$ K, $P = 1$ atm. (b) Drift in thermal conductivity at $T = 298$ K, $P = 1$ atm due to numerical integration of HCACF at larger sampling times.

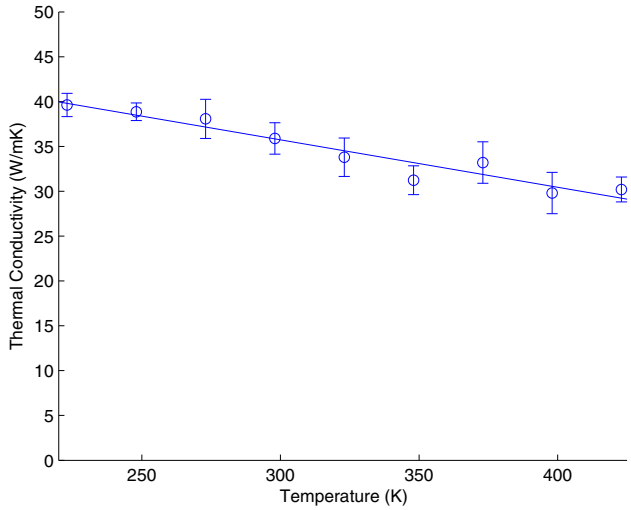

Fig. 12. Thermal conductivity for a SWNT of length 36.89 Å with periodic boundary conditions applied for various temperatures at P = 1 atm.

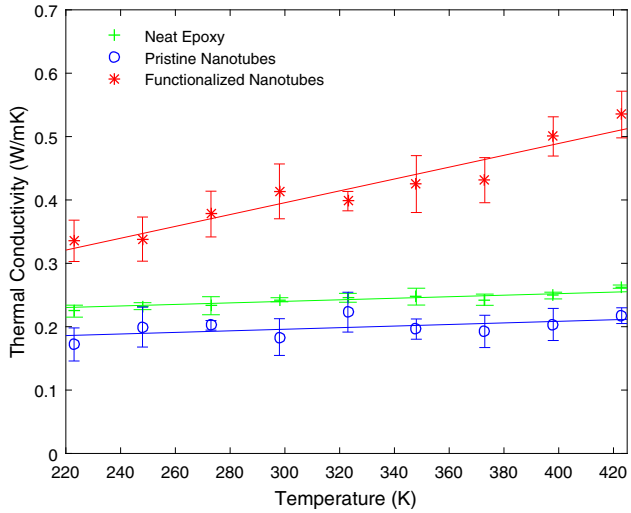

Fig. 13. Thermal conductivity in the directions perpendicular the nanotube axis (x–y plane) for functionalized and pristine SWNT/epoxy nanocomposites compared with neat epoxy.

above in Fig. 12. The functionalized SWNT/epoxy system showed significant improvement (~700%) over neat epoxy in the nanotube direction, as seen in Fig. 14b, but a whole order magnitude lesser than that of the pristine SWNT/epoxy system. Experimenents and simulations have shown that the defects to the nanotube introduced by functionalization decrease the inherent tube thermal conductivity, since they act as scattering points for thermal energy.[11,19] For this reason, it is clear that in regards to overall system thermal conductivity there is a trade-off between the greater improvements along the nanotube direction for the pristine SWNT system, and the improvements perpendicular to the SWNT in functionalized SWNT system. Shenongin et al. proposed that functionalization is only useful for SWNT/epoxy composites containing shorter aspect ratio nanotubes, because reduction in tube conductance is greater in higher aspect ratio SWNTs.[11]

As discussed previously, experimental data has not matched the improvements predicted by simulations, with the likely limitation being inefficient phonon transport between nanotubes. In realistic systems, nanotube ends act as phonon scattering sites, and so discontinuous nanotubes were modeled in this study. This was done by creating nanotubes that did not span the entire simulation cell length. Periodic boundary conditions were still applied, but there is epoxy in-between the nanotubes as shown earlier in Fig. 5b. SWNTs of that span 11/15 of the simulation cell, and 13/15 of the simulation cell are considered. While these are very short SWNTs, they allow the end effects to be investigated as desired. The results for the short nanotubes compared to the infinite systems and neat epoxy, perpendicular to the nanotube axis (x–y plane), and along the nanotube axis (z-direction) in the temperature range of 248–348 K are shown in Figs. 15 and 16, respectively. From Fig. 15, it is seen that the discontinuous functionalized nanotubes have only a slight reduction in thermal conductivity when compared to the infinite epoxy/functionalized system, and the nanotubes spanning 11/15 and 13/15 of the cell show an improvement of 42% over neat epoxy. The discontinuous epoxy/pristine SWNTs systems display higher thermal conductivity compared to the infinite system, and both discontinuous systems are approximately equal to the thermal conductivity of isotropic neat epoxy. This further illustrates that heat transfer to the epoxy perpendicular to the nanotube was poor, and the discontinuous nanotubes allow a larger path, and more epoxy per unit volume for the heat flux to travel around the nanotube. The results along the nanotube axis in Fig. 16 show that for the discontinuous nanotube there is great improvement over neat epoxy, 103% and 115% for the 11/15 and 13/15 cell length pristine SWNT/epoxy systems, and 91% and 103% for the 11/15 and 13/15 cell length functionalized SWNT/epoxy systems. However, gains in thermal conductivity are significantly less than that of the infinite functionalized SWNT/epoxy system. The infinite pristine SWNT/epoxy system is not shown because it yet another order of magnitude greater. This shows that including SWNT end effects drastically lowers the prediction of the thermal conductivity of the SWNT/epoxy nanocomposites. It is further demonstrated that there is a trade-off between the greater improvements along the nanotube direction for the pristine SWNT system, and the improvements perpendicular to the SWNT for the functionalized SWNT system, towards the overall system thermal conductivity.

To simulate an equivalent isotropic system consisting of randomly oriented nanotubes, the thermal conductivity tensors are rotated and averaged over

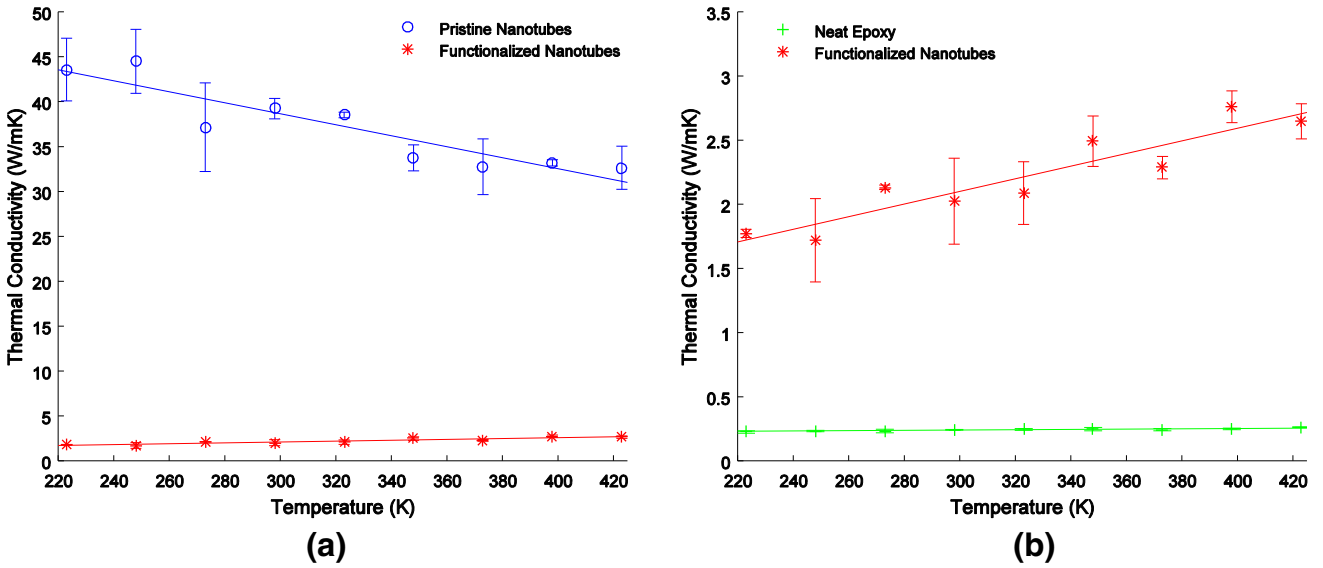

Fig. 14. Thermal conductivity along the nanotube axis (*z*-direction) for (a) pristine SWNT/epoxy nanocomposites compared to functionalized nanocomposite and (b) functionalized SWNT/epoxy nanocomposite compared to neat epoxy.

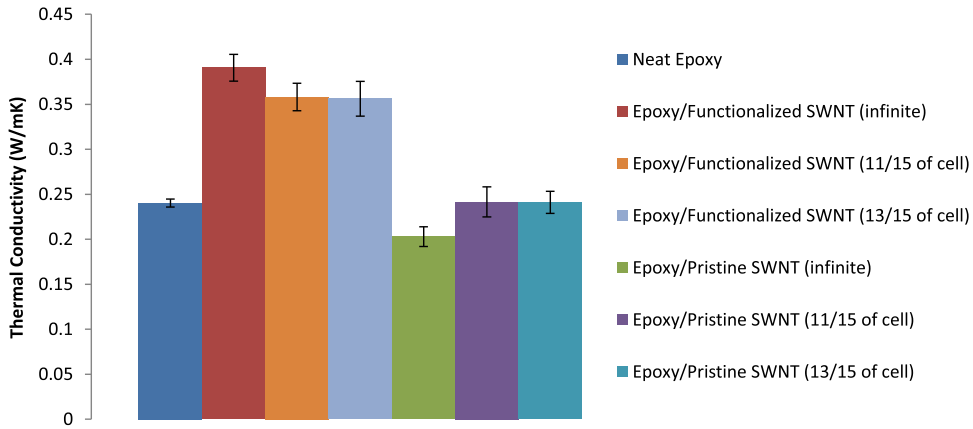

Fig. 15. Thermal conductivity in the temperature range of 248–348 K in the directions perpendicular to the nanotube axis for the various short and infinite SWNT/epoxy nanocomposites studied.

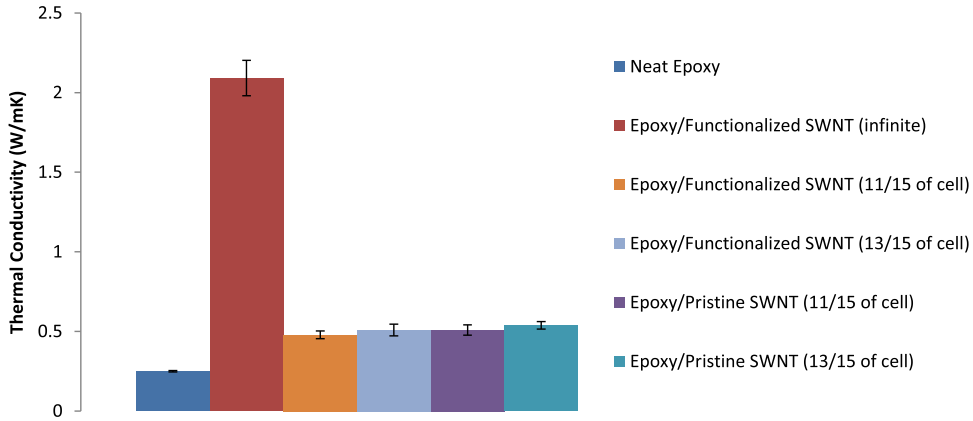

Fig. 16. Thermal conductivity in the temperature range of 248–348 K along the nanotube axis for the various short and infinite SWNT/epoxy nanocomposites studied. Epoxy/Pristine SWNT (infinite) is omitted since its average value is 38.6 W/mK in this temperature range.

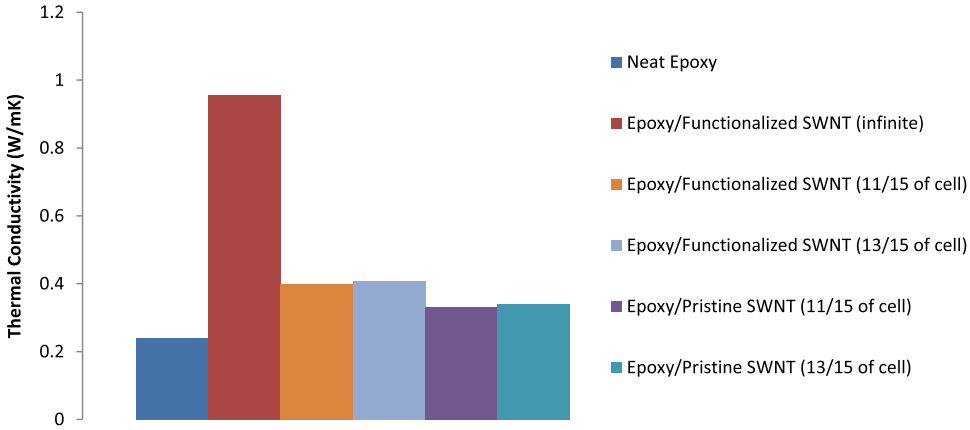

Fig. 17. Thermal conductivity of equivalent isotropic systems created by rotating thermal conductivity tensor over all possible orientations. Epoxy/Pristine SWNT (infinite) is omitted since its equivalent isotropic thermal conductivity is 13 W/mK.

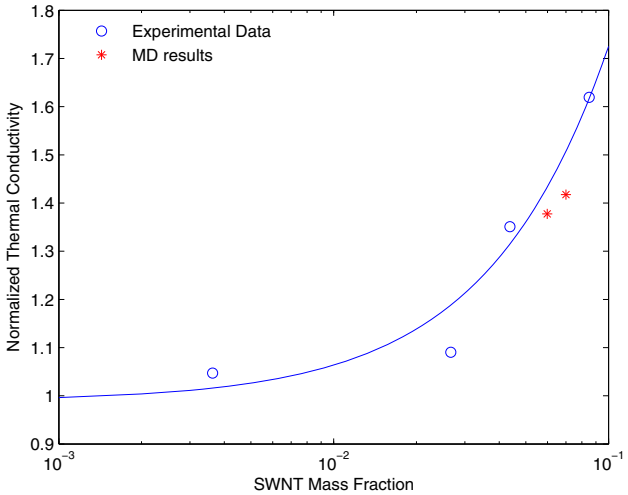

Fig. 18. Experimental comparison of discontinuous pristine SWNT/epoxy composite results at a given mass fraction.[21]

every possible orientation accounting for symmetry, and the results are shown in Fig. 17 for the various nanocomposites. It is highlighted here that for the discontinuous SWNTs, the functionalized system shows a greater improvement in thermal conductivity. The improvements along the nanotube axis are essentially equivalent for the discontinuous pristine and functionalized SWNT/epoxy systems, so the thermal conductivity perpendicular to the SWNT axis being significantly improved by functionalization makes that system superior. However, for the infinite systems, the epoxy/pristine SWNT shows much greater improvement, with an equivalent isotropic thermal conductivity of 13 W/mK. For the long nanotubes, there is a huge reduction in inherent tube conductivity via functionalization. It is expected that the end effects will be of lesser importance for long nanotubes that extend beyond the length of the phonon mean free path, and so inclusion of these effects in the long nanotubes studied is of less importance. This suggests a certain length where the optimum improvement in thermal conductivity transitions from functionalized to pristine SWNTs.

Calculating the equivalent isotropic systems allows a comparison to be done with experiments, since the majority of work has been done with randomly oriented SWNTs. Figure 18 shows the MD results for discontinuous SWNT/epoxy composites at the two different mass fractions compared with experimental data at various mass fractions.[21] The curve shown is from the the effective medium theory fit to the experimental data. Both sets of data were normalized by the value of neat epoxy. The discontinuous nanotubes that span 11/15 and 13/15 of the simulation cell account for mass fractions of 0.06 and 0.07 respectively. The trend shown by increasing the mass faction is in excellent agreement with the experimental data. This confirms that modeling the end effects of the SWNTs is essential to obtaining a realistic prediction of thermal conductivity.

CONCLUSION

Thermal conductivity of crosslinked epoxy and SWNT and epoxy nanocomposites were investigated using MD via the Green–Kubo integral of the heat current auto correlation function. The epoxy network was built using the 'dendrimer' growth approach, and the inclusion of long-range Coulombic interactions via a 'k-space' component of electrostatic energy allows the thermal conductivity to match the experimental value of 0.24 W/mK at room temperature. The use of non-equilibrium methods and periodic boundary conditions has limited many previous studies to calculating interface thermal conductance. In this study, thermal conductivity was calculated in the plane perpendicular to the nanotube, as well as along the nanotube direction. For the pristine, long SWNT/epoxy system, the thermal conductivity along the nanotube direction

is equivalent to that of an isolated SWNT, but in the plane perpendicular to the nanotube sides there is a reduction of 27% when compared to neat epoxy. The functionalized, long SWNT/epoxy system shows a very large increase along the nanotube axis (~700%), though it is an order of magnitude less than that that displayed by the pristine SWNT/epoxy system. The plane perpendicular to the nanotube shows a 64% improvement in thermal conductivity at room temperature when compared to neat epoxy. Inefficient phonon transport between nanotubes at the ends is an important factor in the thermal conductivity of SWNT/epoxy nanocomposites, and for this reason discontinuous nanotubes were investigated. The discontinuous nanotubes show a large improvement over neat epoxy along the nanotube axis, 103–115% for the pristine SWNT/epoxy, and 91–103% for the functionalized SWNT/epoxy systems. The discontinuous, functionalized systems also show a 42% improvement in the plane perpendicular to the nanotube walls, while the discontinuous, pristine SWNT/epoxy systems display no improvement over epoxy. The thermal conductivity tensor is averaged over all possible orientations to allow for experimental comparison, and the results are in excellent agreement for the discontinuous, pristine SWNT/epoxy nanocomposite. For the short nanotubes investigated, functionalization provides greater improvement in overall composite conductivity than pristine nanotubes. For the long nanotubes investigated, the massive increase in the thermal conductivity along the tube boosted composite conductivity much greater than the added improvements in the plane perpendicular to the nanotube due to functionalization when considering deterioration of the inherent tube conductivity. These simulations demonstrate there is a SWNT length threshold where the best improvement for a composite system with randomly oriented nanotubes would transition from functionalized SWNTs to pristine SWNTs.

ACKNOWLEDGEMENTS

The work presented here was supported by Boeing Company (Seattle, WA) and Defense Threat Reduction Agency HDTRA1-13-1-0009. The authors acknowledge the support of the University of Michigan Center for Advanced Computing (CAC), a high-performance computing center located in the Ann Arbor campus.

REFERENCES

1. F.F.T. de Araujo, and H.M. Rosenberg, *J. Phys. D: Appl. Phys*. **9**, 665 (1976).
2. J. Hone, M. Whitney, C. Piskoti, and A. Zettl, *Phys. Rev. B* **59**, 2514 (1999).
3. E. Pop, D. Mann, Q. Wang, K. Goodson, and H. Dai, *Nano Lett*. **6**, 96 (2006).
4. N. Fasanella and V. Sundararaghavan, *Modell. Simul. Mater. Sci. Eng*. **23**, 065003 (2015).
5. R. Kubo, M. Toda, N. Hashitsume, and N. Saito, *Statistical Physics II: Nonequilibrium Statistical Mechanics* (Berlin: Springer, 1985).
6. T. Kawamura, Y. Kangawa, and K. Kakimoto, *Phys. Status Solidi C* **3**, 1695 (2006).
7. P. Chantrenne, M. Raynaud, D. Baillis, and J.L. Barrat, *Microscale Thermophys. Eng*. **7**, 117 (2003).
8. T. Terao, E. Lussetti, and F. Muller-Plathe, *Phys. Rev. E* **75**, 57701 (2007).
9. V. Varshney, S.S. Patnaik, A.K. Roy, and B.L. Farmer. *Polymer* **50**, 3378 (2009).
10. A. Kumar, V. Sundararaghavan, and A.R. Browning, *Modell. Simul. Mater. Sci. Eng*. **22**, 025013 (2014).
11. S. Shenogin, A. Bodapati, L. Xue, R. Ozisik, and P. Keblinski, *Appl. Phys. Lett*. **85**, 2229 (2004).
12. T.C. Clancy, and T.S. Gates, *Polymer* **47**, 5990 (2006).
13. S.T. Huxtable, D.G. Cahill, S. Shenogin, L. Xue, R. Ozisik, Barone, M. Usrey, M. S. Strano, G. Siddons, M. Shim, and P. Keblinski. *Nat. Mater*. **2**, 731 (2003).
14. Z. Xu and M.J. Buehler, *ACS Nano* **3**, 2767 (2009).
15. M. Alaghemandi, F. Mller-Plathe, and M.C. Bhm, *J. Chem. Phys*. **135**, 184905 (2011).
16. V. Varshney, A.K. Roy, T.J. Michalak, J. Lee, and B.L. Farmer, *JOM* **65**, 140 (2012).
17. F.H. Gojny, M.H.G. Wichmann, B. Fiedler, I.A. Kinloch, W. Bauhofer, A.H. Windle, and K. Schulte, *Polymer* **47**, 2036 (2006).
18. M.J. Biercuk, M.C. Llaguno, M. Radosavljevic, J.K. Hyun, A.T. Johnson, and J.E. Fischer, *Appl. Phys. Lett*. **80**, 2767 (2002).
19. C.H. Liu and S.S. Fan, *Appl. Phys. Lett*. **86**, 123106 (2005).
20. E.S. Choi, J.S. Brooks, D.L. Eaton, M.S. Al-Haik, M.Y. Hussaini, H. Garmestani, D. Li, and K. Dahmen, *J. Appl. Phys*. **94**, 6034 (2003).
21. M.B. Bryning, D.E. Milkie, M.F. Islam, J.M. Kikkawa, and A.G. Yodh, *Appl. Phys. Lett*. **87**, 161909 (2005).
22. A. Moisala, Q. Li, I.A. Kinloch, and A.H. Windle, *Compos. Sci. Technol*. **66**, 1285 (2006).
23. A. Bagchi and S. Nomura. *Compos. Sci. Technol*. **66**, 1703 (2006).
24. C. Yu, L. Shi, Z. Yao, D. Li, and A. Majumdar, *Nano Lett*. **5**, 1842 (2005).
25. N. Galamba, C.A. Nieto de Castro, and J.F. Ely *J. Chem. Phys* **120**, 8676 (2004).
26. Q. Wang, B.K. Storm, and L.P. Houmoller. *J. Appl. Polym. Sci*. **87**, 2295 (2003).
27. I. Yarovsky and E. Evans. *Polymer* **43**, 963 (2002).
28. D.R. Rottach, J.G. Curro, J. Budzien, G.S. Grest, C. Svaneborg, and R. Everaers, *Macromolecules* **40**, 131 (2007).
29. D.R. Heine, G.S. Grest, C.D. Lorenz, M. Tsige, and M.J. Stevens, *Macromolecules* **37**, 3857 (2004).
30. C. Wu and W. Xu. *Polymer* **47**, 6004 (2006).
31. S. Christensen, *Proc. of 39th ISTC SAMPE Conf.* (2007).
32. C.K. Knox, J. W. Andzelm, J.L. Lenhart, A.R. Browning, and S. Christensen, *27th Army Science Conf. Proc.* (2010).
33. Accelrys Software Inc., Discovery Studio Modeling Environment: Release 5.5, San Diego (2007).
34. P. Dauber-Osguthorpe, V. A. Roberts, D. J. Osguthorpe, and J. Wolff, *Proteins: Struct., Funct., Genet.*, 4, 31 (1988).
35. S. Plimpton, *J. Comput. Phys*, 117, 1 (1995).
36. D.A. McQuarrie, *Statistical Mechanics* (Sausalito, CA: University Science Books, 2000).
37. A.J.C. Ladd, B. Moran, and W.G. Hoover, *Phys. Rev. B* **34**, 5058 (1986).
38. S. Nose and M.L. Klein, *Mol. Phys*. **50**, 1055 (1983).
39. J. Petravica, *J. Chem. Phys*, 123, 174503 (2005).
40. D.M. Heyes, *Phys. Rev. B* 49, 755 (1994).
41. B.A. Luty, I.G. Tironi, and W.F. van Gunsteren, *J. Chem. Phys* **103**, 3014 (1995).
42. M. Deserno and C. Holm. *J. Chem. Phys*. **109**, 7694 (1998).
43. S. Berber, Y.-K. Kwon, and D. Tomanek, *Phys. Rev. Lett*. **84**, 4613 (2000).
44. J.R. Lukes and H. Zhong, *J. Heat Transf*. **129**, 705 (2007).